Starch functionalized magnetite nanoparticles: New insight into the structural and magnetic properties

Mbolantenaina Rakotomalala Robinson, Mustapha Abdelmoula, Martine Mallet, Romain Coustel

▶ **To cite this version:**

Mbolantenaina Rakotomalala Robinson, Mustapha Abdelmoula, Martine Mallet, Romain Coustel. Starch functionalized magnetite nanoparticles: New insight into the structural and magnetic properties. Journal of Solid State Chemistry, 2019, 277, pp.587-593. 10.1016/j.jssc.2019.06.033 . hal-02184206

HAL Id: hal-02184206
https://hal.science/hal-02184206

Submitted on 25 Oct 2021

HAL is a multi-disciplinary open access archive for the deposit and dissemination of scientific research documents, whether they are published or not. The documents may come from teaching and research institutions in France or abroad, or from public or private research centers.

L'archive ouverte pluridisciplinaire **HAL**, est destinée au dépôt et à la diffusion de documents scientifiques de niveau recherche, publiés ou non, émanant des établissements d'enseignement et de recherche français ou étrangers, des laboratoires publics ou privés.

Distributed under a Creative Commons Attribution - NonCommercial 4.0 International License

Version of Record: https://www.sciencedirect.com/science/article/pii/S0022459619303238
Manuscript_90e408df27f3de00c795f262ec9eee29

Starch functionalized magnetite nanoparticles: new insight into the structural and magnetic properties

Mbolantenaina Rakotomalala Robinson[a], Mustapha Abdelmoula[a], Martine Mallet[a] and Romain Coustel[a,1]

[a]*Laboratoire de Chimie Physique et Microbiologie pour les Matériaux et l'Environnement (LCPME), UMR 7564 CNRS-Université de Lorraine, 405 rue de Vandoeuvre, 54600 Villers-Lès-Nancy, France*

Abstract

In this study we report the preparation of starch-functionalized magnetic nanoparticles (Starch@MNPs) by the oxidation-precipitation method of iron (II). Special attention was devoted to the characterization of the modification of structural and magnetic properties depending on the starch to iron mass ratio R. Transmission electron microscopy (TEM), powder X-ray diffraction (PXRD), Raman, Mössbauer, Fourier transform infrared (FTIR), X-ray photoelectron spectroscopies (XPS) and thermogravimetric analysis (TGA) were used to carefully characterize and compare the as-synthesized products. TEM and PXRD revealed the reduction of the crystallite size as R increases. The size varies from 67 ± 5 to 12 ± 4 nm by changing R from 0 to 10. The formation of a cubic inverse spinel iron oxide phase was demonstrated by PXRD and the discrimination between magnetite Fe_3O_4 and maghemite Fe_2O_3 was realized by Raman and Mössbauer spectroscopy. Mössbauer spectroscopy allowed to monitor the evolution of the magnetic properties with respect to R. The superparamagnetic behaviour was evidenced by the appearance of a doublet in the Mössbauer spectra that strongly increased in intensity with R ratio. The relative abundance (RA) of the doublet at room temperature was observed to increases from 10 to 36 % for R equal 1 to 10. Lastly, the iron environment was highly perturbed by the presence of starch.

Keywords: Magnetic nanoparticles; superparamagnetic materials; magnetite; polysaccharide; Raman; Mössbauer

[1]Corresponding author

Email: romain.coustel@univ-lorraine.fr

© 2019 published by Elsevier. This manuscript is made available under the CC BY NC user license
https://creativecommons.org/licenses/by-nc/4.0/

1. Introduction

The preparation and characterization of magnetic materials at nanoscale attract strong interest because of their properties that differ appreciably with respect to the bulk material. They have many possible uses in the biomedical field as contrast agents in magnetic resonance imaging or as drug delivery systems [1,2], in environmental processes as nano-adsorbents or as catalysts [3–6], in data storage [7], etc.

Magnetite (Fe_3O_4) exhibits one of the largest saturation magnetizations among iron oxides (92 emu g^{-1} at room temperature [8]). It has a face-centered cubic inverse spinel structure and differs from most other iron oxides since it contains both divalent and trivalent iron. Its formula can be written as $Fe_A^{3+}[Fe^{2+}Fe^{3+}]_BO_4$ where A and B denote tetrahedral and octahedral sites respectively [9]. The iron ions in the octahedral sites make fast electron hopping leading to the averaged valence state of $Fe^{2.5+}$. Below 120 K, magnetite undergoes a phase transition from cubic to monoclinic known as the Verwey transition and become an insulator as the electron hopping ceases to occur [10]. The magnetic properties of iron oxides and magnetite in particular are also size-dependent [11]. Large size magnetite crystals have multi-domain magnetic structure and become single domain as the size is reduced below 90 nm. The magnetic moment of the nanoparticles can undergo a spontaneous flip at room temperature as the size continues to decrease at around 30 nm. This gives rise to superparamagnetic characteristic [12].

Various synthesis routes have been developed for the preparation of nanostructured magnetite. The co-precipitation of Fe^{2+} and Fe^{3+} by a base is by far the most synthetic method reported in the literature [13–17]. An alternative consists in the oxidation-precipitation of ferrous salt in alkali aqueous solution but remains less used [18–20] or by reaction of iron oxhyhydroxydes with soluble Fe(II) [21]. Coating of the magnetite surface with organic and/or inorganic material molecules allows tuning structural and magnetic properties of magnetite [22–24]. More recently, the involvement of polysaccharides in magnetite synthesis has been promising at fabricating eco-friendly materials [25–31]. Starch emerges as one of the potential functionalization agents in magnetite synthesis due to its low-toxicity, abundance and cost-effectiveness [32–37]. The available researches have been primarily focused on the technological application aspects and little attention has been paid to understand the effect of such polysaccharide on the structural and magnetic properties of magnetite.

This report presents the successful preparation of starch functionalized nanoparticles via the oxidation-precipitation method. Peculiar attention was paid to both structure and properties of

magnetite particles synthetized with increasing amount of starch. Obtained products were carefully characterized by TEM, PXRD, Raman, FTIR spectroscopies, XPS and TGA. The progressive emergence of the superparamagnetic behaviours of the nanocomposite was probed by Mössbauer spectroscopy.

2. Materials and methods

2.1 Materials

Ferrous sulphate heptahydrate ($FeSO_4 \cdot 7H_2O$), potassium hydroxide (KOH), potassium nitrate (KNO_3), ethanol (96%) and soluble starch were obtained from Fischer Chemical, Riedel-de Haën, Merck, VWR and Sigma-Aldrich, respectively. All chemicals were analytical grade and used as received without further purification. Ultrapure water (18.2 MΩ cm^{-1}) was used for the all experiments. Water was previously bubbled at least 1 hour with N_2 prior to use.

2.2 Synthesis of magnetic nanoparticles (MNPs)

MNPs were prepared following the synthesis of magnetite (Fe_3O_4) by the oxidation-precipitation of ferrous sulphate method as reported by Schwertmann and Cornell [19]. Typically, 80 g of $FeSO_4 \cdot 7H_2O$ were dissolved in 560 mL purified water under magnetic stirring and N_2 atmosphere in a 1 L flask and heated up to 90°C. When the temperature was reached, 240 mL of aqueous solution containing 6.46 g KNO_3 and 44.90 g KOH were added dropwise to the reaction vessel (50 mL min^{-1}) using a peristaltic pump. After the addition of the last drop, the mixture was heated for a further 45 minutes. Then, the mixture was cooled to room temperature overnight. The black precipitate was recovered by centrifugation, washed 5 times with water and then washed 1 time with ethanol (96%, from VWR) to remove the unreacted reagents. The resulting product was dried under vacuum.

The same procedure was used for the synthesis of starch functionalized MNPs (Starch@MNPs) except that starch was added to $FeSO_4$ solution and gelatinized at 90°C before the addition of the KNO_3 and KOH mixture solution. The starch to Fe mass ratio (R) was allowed to vary over the range between 0.05 and 10. The following steps remained the same. The obtained samples were labelled from R0.05 to R10, and the non-functionalized MNPs R0.

2.3 Materials characterization

The morphologies of the as-prepared products were analyzed using transmission electron microscopy (TEM) and high-resolution transmission electron microscopy (HRTEM) on a Philips CM200 and JEOL 2100F respectively operating both at an accelerating voltage of 200 kV. Samples were dispersed in an ethanol solution under sonication and evaporated at room temperature on a carbon-coated copper grid.

The identification of crystalline structure of the synthesized nanoparticles was performed by powder X-ray diffraction (PXRD) using a PANalytical X'Pert MDP diffractometer equipped with a Cu Kα radiation source and a rapid X'Celerator detector.

Raman spectra were recorded using a Jobin Yvon T64000 spectrometer equipped with a 532 nm laser through a ×50 microscope objective. The power of the laser was set to 600 mW. To prevent the oxidation of the sample, the power of the laser beam was reduced by means of a series of neutral density filters.

^{57}Fe Mössbauer spectra were collected using a conventional spectrometer in transmission geometry coupled with a cold head cryostat from Advances Research Systems (USA), equipped with vibration isolation stand, developed in LCPME laboratory. The 50 mCi ^{57}Co in Rh matrix radioactive source was mounted in a constant acceleration velocity transducer. Measurements were taken at the wide range of velocity ± 11 mm s^{-1}. The hyperfine interaction parameters were determined by fitting the experimental spectra by a least-squares method using the Recoil software [38]. The center shifts were reported with respect to that of 25 µm-thick α-Fe foil at room temperature.

3. Results and discussion

3.1 TEM

Morphological study of the as-prepared nanoparticles was carried out using TEM. Figure 1 shows examples of TEM and HRTEM micrographs and selected area electron diffraction (SAED) patterns of the R0 and R10 samples.

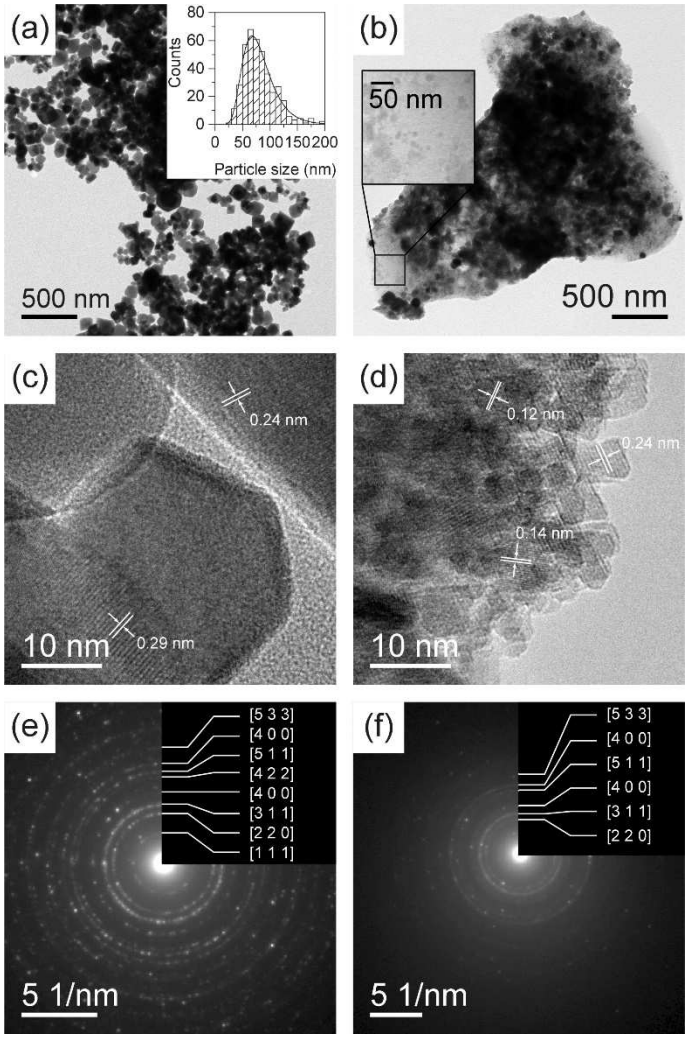

Figure 1. TEM micrographs of R0 (a) and R10 (b); HRTEM micrographs of R0 (c) and R10 (d); SAED patterns of R0 (e) and R10 (f). The inset image in panel (a) refers to the particle sizes distribution fitted with Log-normal profile.

As illustrated, on the one hand, R0 was composed mostly of cubic shape nanoparticles along with some minor hexagonal shape (figure 1(a) and (c)) in the wide size range of about 20 to 200 nm. The particle size obtained by oxidation-precipitation method were relatively high compared to the size obtained by co-precipitation which is around 10 to 40 nm [39–41]. The HRTEM micrograph (figure 1(c)) of the same sample revealed clearly parallel lattice fringes, indicating the high crystallinity of the nanoparticles. The measured inter-fringe distances of about 0.24 and 0.29 nm were consistent with cubic spinel iron oxides as discussed latter (see section 3.2) and can be assigned to the inter-planar distances of the (222) and (220) crystallographic planes of magnetite (JCPDS data 19-0629) respectively. Each grain constituting R0 appeared to be a single crystal (figure 1(c)) with smooth edges. The corresponding SAED of R0 (figure 1(e)) displays a spotty ring pattern characteristic of single crystal specimen present in few numbers and randomly oriented in the selector aperture [42].

The indexed rings were in good agreement with PXRD analyses discussed below. On the other hand, R10 may be assimilated as a big flake of starch containing nanoparticles dispersed inside (figure 1(b)). Two different objects may be distinguished: small nanoparticles of about 10 nm that can be seen on the clear part of the polymer matrix (area surrounded by square in figure 1(b)) and larger nanoparticles in the same order of size as in R0. Thorough observation of HRTEM micrograph (figure 1(d)) revealed the main difference of R10 in comparison with R0. When considering a fairly large grain in R10, it seems that it is constituted of nano-grains gathered in a cluster forming a polycrystalline specimen that contributes to the formation of continuous rings in the SAED pattern (figure 1(f)). Lattice fringes corresponding to the crystallographic planes (444), (531) and (222) (d_{hkl} ~ 0.12, 0.14 and 0.24 nm respectively) characteristics of magnetite (JCPDS data 19-0629) were also identified. SAED pattern of R10 exhibited fewer rings in regard to R0 but the indexed rings remained consistent with the cubic spinel iron oxides and were in good agreement with PXRD results discussed below. The presence of starch affects then drastically the MNPs's morphology by the extinction of some diffraction rings but the cubic spinel order is maintained.

3.2 PXRD

The phases composing the as-synthesized product were identified by PXRD. Figure 2 shows the obtained diffractograms.

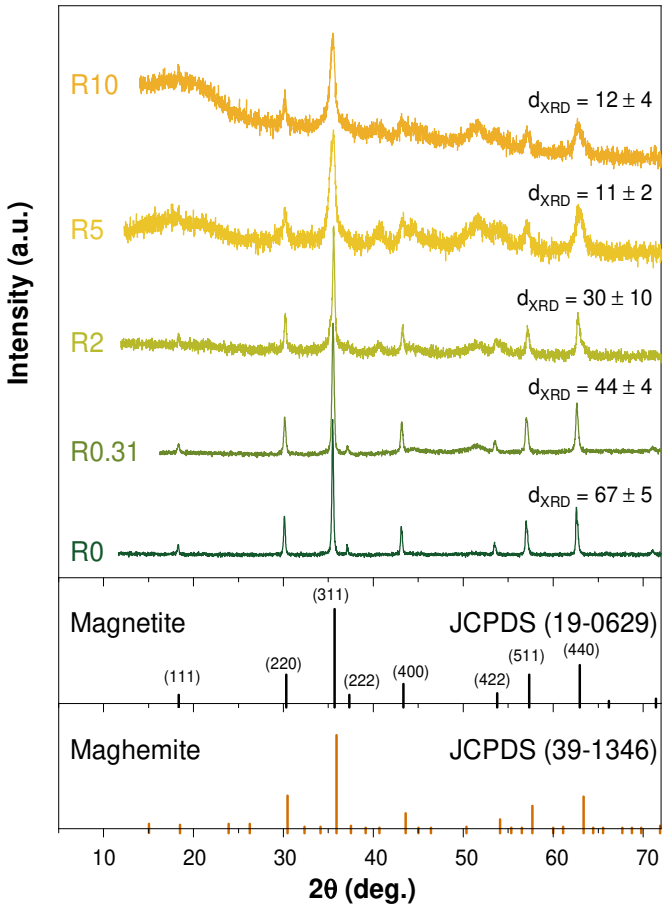

Figure 2. PXRD patterns of the as-synthetized products at different R values; d_{XRD} denotes the crystallite size calculated from Scherrer's formula in nm.

Considering the diffraction pattern of R0, all the reflection peaks can be indexed within the cubic spinel structure of magnetite (JCPDS data n° 19-0629) corroborating the results of HRTEM and SAED mentioned above. Spinel structure of MNPs was essentially maintained for R0.31-10 samples as the diffraction peak positions remained unchanged. The presence of amorphous starch leads to an additional broad peak at 2θ range of 15-25° for samples with high R value (R5-10). Two peaks appeared at 2θ equals to 40.7 and 51.6° and may be ascribed tentatively to δ-FeOOH impurity. From the diffraction patterns, it was also observed a broadening trend of the reflection peaks with the increase of R value, indicating the reduction of the crystallite size of magnetite. The average crystallite sizes were estimated by applying Scherrer's formula (Equation (1)) [43,44] on the two most intense peaks (311) and (440) after Kα2 stripping using X'Pert Highscore Plus v2.2b software.

$$d_{XRD} = \frac{k\lambda}{B_r \cos\theta} \qquad (1)$$

where k is the shape factor and equals to 0.89 for spherical particles, λ is the wavelength of Cu-Kα1 radiation, θ is the diffraction angle and B_r the geometric mean of the full width at half

maximum (FWHM) of the observed peak B_0 and the FWHM due to instrumental effects B_i (measured from the diffractogram of size and strain effect-free LaB_6 standard):

$$B_r = \sqrt{(B_0 - B_i)\sqrt{(B_0^2 - B_i^2)}} \qquad (2)$$

The average sizes of the crystallites (d_{XRD}) of all samples are shown in figure 2 and were estimated to be 67 ± 5, 44 ± 4, 30 ± 10, 11 ± 2 and 12 ± 4 nm for R0, R0.31, R2, R5 and R10 respectively. The crystallite sizes showed a decreasing trend with the increase of R. Interestingly, a limited amount of starch (R0.31) in the synthetic medium leads to abrupt drop of the crystallite size from 67 nm to 44 nm. This suggests that starch may serve as nucleation points, enhancing the number of small crystallites. At higher R further crystallite size reduction is observed. One may also suspect starch to induce defaults in magnetite structure, e.g. polymer chain embedment in oxide, contributing to lower the size of coherently diffracting domains. In the case of R0, the calculated d_{XRD} was in fair agreement with TEM observations where the distribution curve indicates an average size of 80 ± 30 nm. For the R10, the estimation of grain size from TEM was difficult which justified the use of indirect technique like PXRD. By varying the value of R, one can successfully evolves the size of the MNPs.

It is worth noting that the structure of magnetite and maghemite are very similar. Hence, the discrimination of the two phases was not easy by mean of PXRD. The main difference lies in the low Bragg angle where few extra peaks are only present for the maghemite (JCPDS data 39-1346). The intensities of theses peaks are very weak that makes the identification of maghemite difficult. Further characterization by Raman or Mössbauer spectroscopies should be performed to distinguish the iron oxide phases as these latter exhibit distinct Raman active phonon modes and distinct hyperfine parameters.

3.3 Raman spectroscopy

Raman spectroscopy is a reliable technique which allows a discrimination among the different phases of iron oxides [45]. The Raman spectra of all samples are illustrated in figure 3.

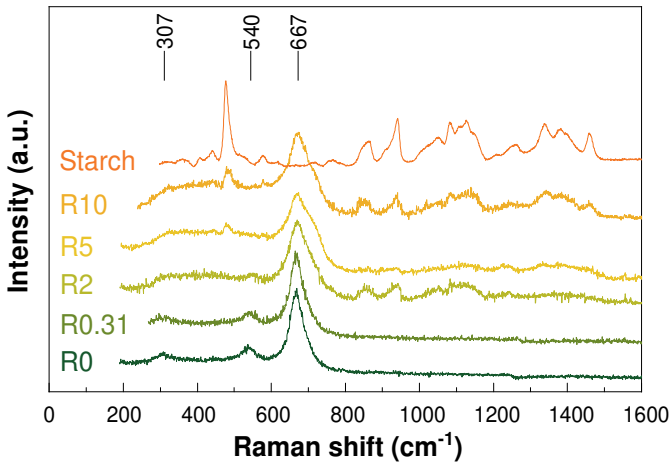

Figure 3. Raman spectra of the as-synthesized products at different R values and native starch.

The main bands corresponding to A_{1g}, T_{2g} and E_g modes of magnetite were clearly evidenced for the sample R0 at 667, 540 and 307 cm^{-1} respectively. The band positions were in good agreement with literature values [45,46]. The weak T_{2g} and E_g bands overlapped with starch characteristic bands in the range of 200-600 cm^{-1} when starch content exceeds R2. The band centered at 667 cm^{-1} widened as the ratio R increased which was indicative of particle size reduction induced effect or appearance of disorder [47] in accordance with the PXRD characterizations. The bands originating from starch were not well resolved and further characterization with FTIR and XPS were performed (see Supporting Information). Both FTIR and XPS highlighted the success of functionalization. Starch contribution to FTIR or XPS spectra clearly increases with R (figures S1 and S2, Supporting Information). Both techniques evidenced that no chemical modification of starch took place during the synthesis. The only change observed in starch FTIR fingerprint can be attributed to a slight modification of starch crystallinity. The Raman characterization provides evidence on the formation of magnetite as the main iron oxide phase by the synthesis method used in the present study regardless the perturbation induced by starch.

3.4 Mössbauer spectroscopy

Mossbauer spectroscopy has been used to investigate the structural together with magnetic properties of the as synthetized products. The Mössbauer spectra recorded at room temperature (RT) for different samples are shown in figure 4(a), and the corresponding hyperfine parameters in table 1.

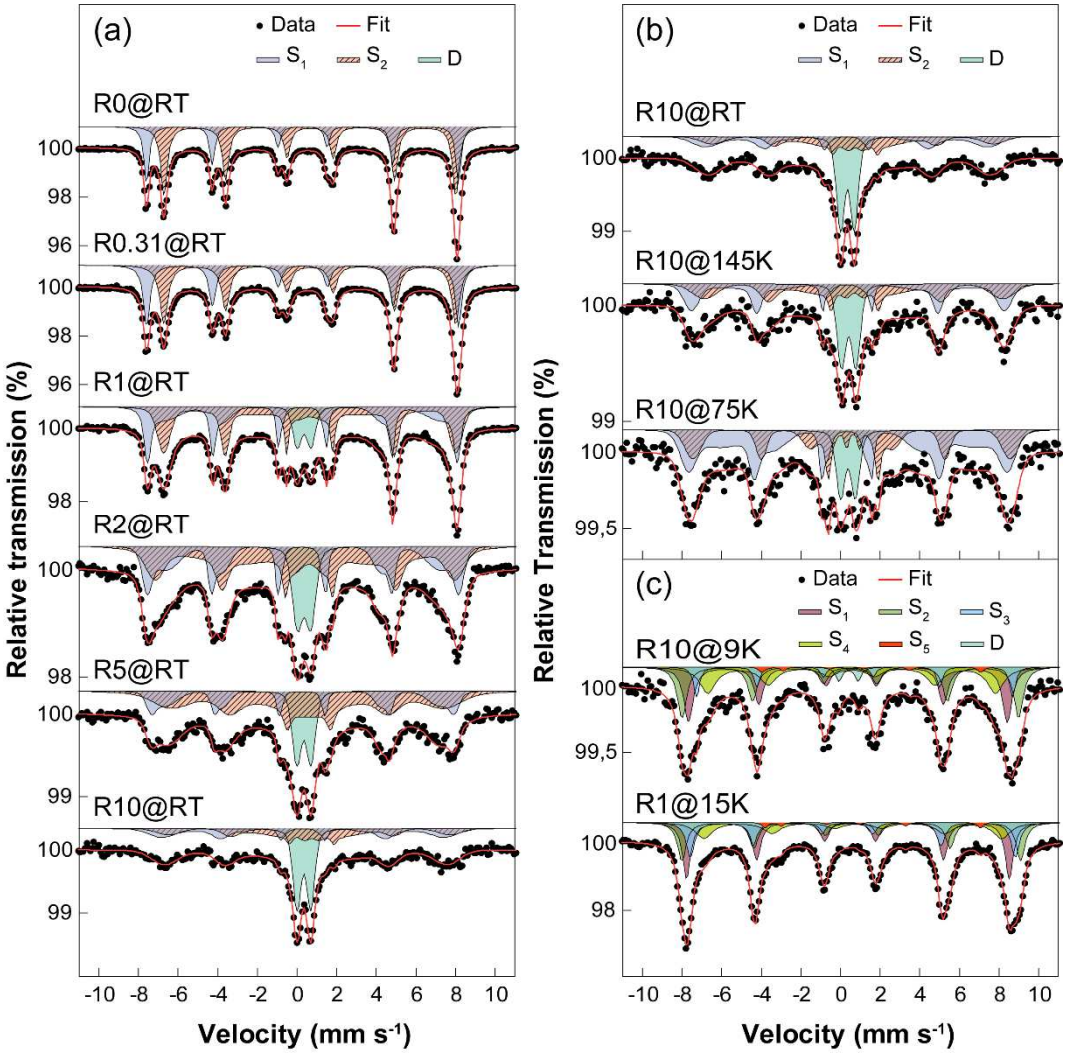

Figure 4. Mössbauer spectra of the as-synthetized products at different R values recorded at room temperature (a); Mössbauer spectra of R10 between room temperature and 75 K (b) and Mössbauer spectra of R10 and R1 at 9 K and 15 K, respectively (c).

The MNPs sample R0 exhibits two narrow sextets. The outer sextet with CS = 0.28 mm s^{-1}, H_{eff} = 48.8 T and small quadrupole shift (ε) was assigned to high spin Fe^{3+} in tetrahedral site and the inner one with CS = 0.66 mm s^{-1}, H_{eff} = 45.7 T and also a small ε to mixed valence $Fe^{2.5+}$ in octahedral site noted as S_1 and S_2 respectively. These values were in good agreement with results obtained for well-crystallized bulk magnetite [49] and corroborated the results obtained by Raman spectroscopy. From the relative area (RA) of S_1 and S_2, the deviation from ideal stoichiometry δ of magnetite ($Fe_{3-\delta}O_4$) was determined according to the recommendations of Zegeye et al [50]. The obtained δ value for R0 was equal to 0.02 indicating that the sample was very close to pristine magnetite, while a bit higher deviation from ideal stoichiometry δ = 0.06 was determined for R0.31. It has to be noticed that Lorentzian multiplet analysis model was used in recoil software [38] as a fitting procedure for the spectra of R0 and R0.31. In contrast, at higher value of R (1-10) the Mössbauer spectra

become more complex, with the emergence of quadrupole doublet as well as the significant broadening of the sextets, suggesting a thermal relaxation effects [51]. The broadening of the sextet lines is thereby modelled by hyperfine field distributions (HFDs) and the Voig-based fitting (VBF) analysis was used to extract characteristic spectral parameters [38,52]. The experimental spectra for samples R1 to R10 were fitted with one quadrupole doublet and 2 HFDs. The gradual evolution from a Lorentzian multiplet characterizing a long-range magnetic order (samples R(0-0.31)) to more complex spectra with superposition of broad sextet components and doublet in which long-range magnetic order is absent can be attributed to the dynamic effects resulting from the fluctuations in the local environment of the probe nucleus (*i.e.* Fe), such as those arising from superparamagnetism [53]. It is known from the literature that when the MNPs size decreases below a certain value, the magnetic moment of such nanoparticles are subject of spontaneous flip and exhibit superparamagnetic behaviours [54]. The time constant of this process is the Néel relaxation time (τ_N):

$$\tau_N = \tau_0 e^{\frac{KV}{k_B T}} \qquad (3)$$

where τ_0 is a constant in the range of 10^{-9}-10^{-12} s depending on the material, K the magnetic anisotropy constant, V the particle volume, k_B the Boltzmann's constant, and T the temperature. If τ_N becomes lower than the Mössbauer measurement time ($\tau_N < 10^{-10}$ s) the magnetically split spectra collapse into one or two paramagnetic lines and in the intermediate range of relaxation times, the spectra present a very broad lines with gradual transition from a sextet to a doublet [51,53]. In the present study, the shape of the Mössbauer spectra of R(1-10) suggests a broad distribution of particles sizes with different relaxation times. The quadrupole doublet may arise from the very small MNPs diluted in the starch matrix, and the broad sextets from bigger MNPs and/or aggregated very small MNPs with higher relaxation times corroborating the TEM observations of R10. The relative abundance of the doublet (RA(D)) gradually increases with starch amount from 10 to 36% for R1 to R10 respectively. One can assume that in addition to the role of starch in the reduction of crystallites sizes, the latter can also allow to better disperse the MNPs. Also, the average hyperfine fields $\langle H_{hf} \rangle$ for S_1 and S_2 were reduced as the R value increases.

To better understand the dynamic magnetic behaviours of starch@MNPs, Mössbauer measurements at different temperatures were also performed. Figure 4(b-c) shows the evolution with temperature of the sample R10 spectrum. While the fitting procedure was the same as for RT for 145 and 75 K, at 9K five Lorentzian shaped sextets were used to reproduce the magnetic component as established for magnetite at low temperature where the structure is

no longer cubic but monoclinic [55–57] and one quadrupole doublet for the residual superparamagnetic contribution. The spectra for R1 at 15K is supplied for comparison (figure 4(c)).

It was shown that the spectra evolve gradually when the temperature decreases. The magnetic contribution increases progressively, while the relative abundance of the doublet decreases from 36 to 3% between RT and 9 K (figure S4, Supporting Information). This change could be connected to the reduction of the thermal relaxation effects. It indicates that we approach the blocking temperature T_B where the magnetization of single domain particle is fixed along its easy axis, in a blocked state [58]. As temperature increases, the magnetic moment will oscillate around the easy axis with larger amplitude as it gets warmer, until it starts to jump over the energy barrier between the two easy directions with relaxation time τ_N. However, only dilute fine particle systems with a narrow distribution of particle sizes, where interparticle interactions can be considered absent, have spectra properly modelled. It consists of a sum of magnetic sextet and doublet with a temperature dependent area ratio resulting of superparamagnetic relaxation. The definition of T_B which depends upon equal areas of sextet and doublet, is useful for such spectra [59]. However, among the abundant literature of these decades on the dynamics of magnetics nanoparticles, van Lierop and Ryan [60] suggest a more robust definition of T_B from a multilevel relaxation model. Concerning R10 with distribution of particle sizes, the simplest model fails and it becomes difficult to predict T_B [51]. Similarly, RA(D) decreases with decreasing temperature for R1 and R2 samples (figure S4, Supporting Information) confirming that T_B decreases with increasing R.

At very low temperature, the five sextet components can be attributed to Fe^{3+} in one tetrahedral site and both Fe^{3+} and Fe^{2+} in octahedral sites. The presence of the prominent features, specifically the hyperfine parameters of the sextet S_5 (high CS~1mm s^{-1}, high quadrupole shift 2ε>1 mm s^{-1} and low magnetic hyperfine field ~34 T) suggests the presence of Fe^{2+} in octahedral sites and confirms the formation of magnetite which is not obvious at RT. To ensure this assumption, a 1,10-phenantroline assay has been done on the sample R10. The formation of orange-red complex testifies the presence of Fe^{2+}. By comparing the spectra of R10 and R1 at 9 and 15 K respectively, the spectrum of R10 appears to be broader. At these temperatures, the broadening from the thermal relaxation effects can be considered as negligible which allow us to assume that the broadening arises from the disorders in the atomic environment of iron atoms that is more important in R10. Then, starch highly influences the iron environments of magnetite.

Table 1. Mossbauer hyperfine parameters for the as-synthetized products at different R values obtained after fitting the experimental data.

Sample	Site	CS (mm s^{-1})	Δ or ε (mm s^{-1})	H_{hf} or $\langle H_{hf} \rangle$ (T)	RA (%)	δ
R0@RT	S_1	0.28	0.00	48.8	38	0.02
	S_2	0.66	-0.01	45.7	62	
R0.31@RT	S_1	0.29	0.00	48.8	44	0.06
	S_2	0.66	-0.01	45.7	56	
R1@RT	D	0.36	0.70	-	10	
	S_1	0.28	0.00	45.9	40	
	S_2	0.65	0.00	38.5	50	
R1@15K	S_1	0.43	-0.06	50.5	33	
	S_2	0.56	-0.02	53.0	24	
	S_3	0.47	0.15	50.9	21	
	S_4	0.76	-0.14	46.6	20	
	S_5	0.90	0.70	33.7	2	
R2@RT	D	0.36	0.69	-	15	
	S_1	0.28	0.03	45.3	35	
	S_2	0.51	-0.10	36.9	50	
R5@RT	D	0.35	0.70	-	17	
	S_1	0.28	0.01	44.4	24	
	S_2	0.56	-0.04	35.1	59	
R10@RT	D	0.35	0.69	-	36	
	S_1	0.29	-0.01	41.7	29	
	S_2	0.68	-0.06	26.3	35	
R10@145K	D	0.41	0.73	-	25	
	S_1	0.36	0.02	44.7	37	
	S_2	0.68	-0.03	33.7	39	
R10@75K	D	0.37	0.74	-	13	
	S_1	0.34	0.03	44.1	55	
	S_2	0.59	-0.04	36.4	32	
R10@9K	D	0.40	1.00	-	3	
	S_1	0.45	-0.08	49.9	31	
	S_2	0.49	0.01	52.7	29	
	S_3	0.55	0.16	49.5	10	
	S_4	0.56	-0.03	45.1	25	
	S_5	0.90	1.00	34.0	2	

CS: center shift relative to alpha-iron, Δ: quadrupole splitting of paramagnetic component, ε: quadrupole shift, H_{hf}: hyperfine field (average value in case of distribution $\langle H_{hf} \rangle$), RA: relative abundance of each site and δ: deviation from stoichiometry.

Conclusion

We have successfully synthetized and *in-situ* functionalized magnetite with starch via an oxidation-precipitation of Fe(II) which constitutes an alternative way to the usual coprecipitation method. The effect of starch on the structural and magnetic properties of the as synthesized products has been extensively investigated using a wide range of characterization techniques. We evidenced that starch plays a significant role in the modification of magnetite properties compared to the non-functionalized bulk phase. TEM and XRD analyses revealed that small particles were obtained in the presence of starch and the size decreases with the quantity of starch expressed as the starch to iron mass ratio R. The crystallite size varies from 66 ± 5 nm for R0 to 12 ± 4 nm for R10. The formation of cubic spinel structure phases was confirmed by SAED, XRD and Mössbauer spectroscopy. Stoichiometric magnetite was found to be the main phase formed at low values of R, while oxidation and disorder accompanied particle size reduction at higher R values as evidenced by Raman and Mössbauer spectroscopy. The reduction of the crystallite size is also accompanied by the appearance of superparamagnetic behaviour supported by the presence of the doublet and the asymmetric broadening of the magnetic component in the Mössbauer spectra as the value of R increases. The superparamagnetic doublet represents 10 % for R1 and increases up to 36 % for R10. The presence of starch leads also to the perturbation of the iron environments conducting to the distribution of the hyperfine fields of the spectra. FTIR and XPS fingerprints of starch in Starch@MNPs appear similar to those of native starch. Finally, we expect that the possibility to tailor magnetite properties with starch which can be also extended to other polymers opens up several possibilities of application for this type of nanomaterial. For this purpose, the use of starch@MPNs to recover pollutants from water are currently under investigation in our laboratory.

Acknowledgements

The authors would like to thank Corine Bouillet (IPCMS-Starsbourg), Sylvie Migot (IJL-Nancy) and Jaafar Ghanbaja (IJL-Nancy) for TEM imaging; Ghouti Medjahdi (IJL-Nancy) and Pierrick Durand (CRM2-Nancy) for PXRD characterizations and Aurélien Renard (LCPME-Nancy) for XPS analyses .

References

[1] J. Hong, D. Xu, J. Yu, P. Gong, H. Ma, S. Yao, Facile synthesis of polymer-enveloped ultrasmall superparamagnetic iron oxide for magnetic resonance imaging, Nanotechnology. 18 (2007) 135608. doi:10.1088/0957-4484/18/13/135608.

[2] J. Zhang, M.C. Shin, A.E. David, J. Zhou, K. Lee, H. He, V.C. Yang, Long-Circulating Heparin-Functionalized Magnetic Nanoparticles for Potential Application as a Protein Drug Delivery Platform, Mol. Pharmaceutics. 10 (2013) 3892–3902. doi:10.1021/mp400360q.

[3] G. Ren, X. Wang, P. Huang, B. Zhong, Z. Zhang, L. Yang, X. Yang, Chromium (VI) adsorption from wastewater using porous magnetite nanoparticles prepared from titanium residue by a novel solid-phase reduction method, Science of The Total Environment. 607–608 (2017) 900–910. doi:10.1016/j.scitotenv.2017.06.103.

[4] Y. Yoon, M. Zheng, Y.-T. Ahn, W.K. Park, W.S. Yang, J.-W. Kang, Synthesis of magnetite/non-oxidative graphene composites and their application for arsenic removal, Separation and Purification Technology. 178 (2017) 40–48. doi:10.1016/j.seppur.2017.01.025.

[5] S.J. Iyengar, M. Joy, A.P. Mohamed, S. Samanta, C.K. Ghosh, S. Ghosh, Fabrication of magnetite nanocrystals in alcohol/water mixed solvents: catalytic and colloid property evaluation, RSC Adv. 6 (2016) 60845–60855. doi:10.1039/C6RA11225K.

[6] A. Bée, L. Obeid, R. Mbolantenaina, M. Welschbillig, D. Talbot, Magnetic chitosan/clay beads: A magsorbent for the removal of cationic dye from water, Journal of Magnetism and Magnetic Materials. 421 (2017) 59–64. doi:10.1016/j.jmmm.2016.07.022.

[7] G.I. Frolov, Film carriers for super-high-density magnetic storage, Tech. Phys. 46 (2001) 1537–1544. doi:10.1134/1.1427988.

[8] K.H.J. Buschow, Handbook of Magnetic Materials, Elsevier, 2006.

[9] R.M. Cornell, U. Schwertmann, The Iron Oxides: Structure, Properties, Reactions, Occurrences and Uses, John Wiley & Sons, 2006.

[10] E.J.W. Verwey, P.W. Haayman, Electronic conductivity and transition point of magnetite ("Fe3O4"), Physica. 8 (1941) 979–987. doi:10.1016/S0031-8914(41)80005-6.

[11] J.L. Dormann, D. Fiorani, E. Tronc, Magnetic Relaxation in Fine-Particle Systems, in: Advances in Chemical Physics, John Wiley & Sons, Ltd, 2007: pp. 283–494. doi:10.1002/9780470141571.ch4.

[12] S. Si, A. Kotal, T.K. Mandal, S. Giri, H. Nakamura, T. Kohara, Size-Controlled Synthesis of Magnetite Nanoparticles in the Presence of Polyelectrolytes, Chem. Mater. 16 (2004) 3489–3496. doi:10.1021/cm049205n.

[13] J.-P. Jolivet, É. Tronc, C. Chanéac, Synthesis of iron oxide-based magnetic nanomaterials and composites, Comptes Rendus Chimie. 5 (2002) 659–664. doi:10.1016/S1631-0748(02)01422-4.

[14] S. Sun, H. Zeng, Size-Controlled Synthesis of Magnetite Nanoparticles, J. Am. Chem. Soc. 124 (2002) 8204–8205. doi:10.1021/ja026501x.

[15] D. Forge, A. Roch, S. Laurent, H. Tellez, Y. Gossuin, F. Renaux, L. Vander Elst, R.N. Muller, Optimization of the Synthesis of Superparamagnetic Contrast Agents by the Design of Experiments Method, J. Phys. Chem. C. 112 (2008) 19178–19185. doi:10.1021/jp803832k.

[16] C.L. Altan, S. Bucak, The effect of Fe 3 O 4 nanoparticles on the thermal conductivities of various base fluids, Nanotechnology. 22 (2011) 285713. doi:10.1088/0957-4484/22/28/285713.

[17] F. Yazdani, M. Seddigh, Magnetite nanoparticles synthesized by co-precipitation method: The effects of various iron anions on specifications, Materials Chemistry and Physics. 184 (2016) 318–323. doi:10.1016/j.matchemphys.2016.09.058.

[18] T. Sugimoto, E. Matijević, Formation of uniform spherical magnetite particles by crystallization from ferrous hydroxide gels, Journal of Colloid and Interface Science. 74 (1980) 227–243. doi:10.1016/0021-9797(80)90187-3.

[19] U. Schwertmann, R.M. Cornell, Iron Oxides in the Laboratory: Preparation and Characterization, John Wiley & Sons, 2008.

[20] L. Gu, H. Shen, Facile one-pot synthesis of multi-armed Fe3O4 nanocrystals, Journal of Alloys and Compounds. 472 (2009) 50–54. doi:10.1016/j.jallcom.2008.04.019.

[21] M. Usman, M. Abdelmoula, K. Hanna, B. Grégoire, P. Faure, C. Ruby, FeII induced mineralogical transformations of ferric oxyhydroxides into magnetite of variable stoichiometry and morphology, Journal of Solid State Chemistry. 194 (2012) 328–335. doi:10.1016/j.jssc.2012.05.022.

[22] K.C. Souza, G. Salazar-Alvarez, J.D. Ardisson, W.A.A. Macedo, E.M.B. Sousa, Mesoporous silica–magnetite nanocomposite synthesized by using a neutral surfactant, Nanotechnology. 19 (2008) 185603. doi:10.1088/0957-4484/19/18/185603.

[23] M. Mikhaylova, D.K. Kim, N. Bobrysheva, M. Osmolowsky, V. Semenov, T. Tsakalakos, M. Muhammed, Superparamagnetism of Magnetite Nanoparticles: Dependence on Surface Modification, Langmuir. 20 (2004) 2472–2477. doi:10.1021/la035648e.

[24] R.C.S. Azevedo, R.G. Sousa, W. a. A. Macedo, E.M.B. Sousa, Combining mesoporous silica–magnetite and thermally-sensitive polymers for applications in hyperthermia, J Sol-Gel Sci Technol. 72 (2014) 208–218. doi:10.1007/s10971-014-3307-7.

[25] A.T. Paulino, A.R. Fajardo, A.P. Junior, E.C. Muniz, E.B. Tambourgi, Two-step synthesis and properties of a magnetic-field-sensitive modified maltodextrin-based hydrogel, Polym. Int. 60 (2011) 1324–1333. doi:10.1002/pi.3084.

[26] H. Dou, B. Xu, K. Tao, M. Tang, K. Sun, The one-pot synthesis of dextran-based nanoparticles and their application in in-situ fabrication of dextran-magnetite nanocomposites, J Mater Sci: Mater Med. 19 (2007) 2575–2580. doi:10.1007/s10856-007-3202-7.

[27] A.K. Hauser, R. Mathias, K.W. Anderson, J. Zach Hilt, The effects of synthesis method on the physical and chemical properties of dextran coated iron oxide nanoparticles, Materials Chemistry and Physics. 160 (2015) 177–186. doi:10.1016/j.matchemphys.2015.04.022.

[28] A.L. Daniel-da-Silva, S. Fateixa, A.J. Guiomar, B.F.O. Costa, N.J.O. Silva, Tito Trindade, B.J. Goodfellow, A.M. Gil, Biofunctionalized magnetic hydrogel nanospheres of magnetite and κ-carrageenan, Nanotechnology. 20 (2009) 355602. doi:10.1088/0957-4484/20/35/355602.

[29] B. Unal, M.S. Toprak, Z. Durmus, H. Sözeri, A. Baykal, Synthesis, structural and conductivity characterization of alginic acid–Fe3O4 nanocomposite, J Nanopart Res. 12 (2010) 3039–3048. doi:10.1007/s11051-010-9898-1.

[30] V.A.J. Silva, P.L. Andrade, M.P.C. Silva, A. Bustamante D., L. De Los Santos Valladares, J. Albino Aguiar, Synthesis and characterization of Fe3O4 nanoparticles coated with fucan polysaccharides, Journal of Magnetism and Magnetic Materials. 343 (2013) 138–143. doi:10.1016/j.jmmm.2013.04.062.

[31] P.R. Chang, J. Yu, X. Ma, D.P. Anderson, Polysaccharides as stabilizers for the synthesis of magnetic nanoparticles, Carbohydrate Polymers. 83 (2011) 640–644. doi:10.1016/j.carbpol.2010.08.027.

[32] N.H. Abdullah, K. Shameli, E.C. Abdullah, L.C. Abdullah, A facile and green synthetic approach toward fabrication of starch-stabilized magnetite nanoparticles, Chinese Chemical Letters. (n.d.). doi:10.1016/j.cclet.2017.02.015.

[33] J.-S. Jiang, Z.-F. Gan, Y. Yang, B. Du, M. Qian, P. Zhang, A novel magnetic fluid based on starch-coated magnetite nanoparticles functionalized with homing peptide, J Nanopart Res. 11 (2009) 1321–1330. doi:10.1007/s11051-008-9534-5.

[34] M. Zhang, G. Pan, D. Zhao, G. He, XAFS study of starch-stabilized magnetite nanoparticles and surface speciation of arsenate, Environmental Pollution. 159 (2011) 3509–3514. doi:10.1016/j.envpol.2011.08.017.

[35] P. Tancredi, S. Botasini, O. Moscoso-Londoño, E. Méndez, L. Socolovsky, Polymer-assisted size control of water-dispersible iron oxide nanoparticles in range between 15 and 100 nm, Colloids and Surfaces A: Physicochemical and Engineering Aspects. 464 (2015) 46–51. doi:10.1016/j.colsurfa.2014.10.001.

[36] K.I. Shingel, R.H. Marchessault, Iron-Polysaccharide Composites for Pharmaceutical Applications, in: Polysaccharides for Drug Delivery and Pharmaceutical Applications, American Chemical Society, 2006: pp. 271–287. http://dx.doi.org/10.1021/bk-2006-0934.ch014.

[37] D.K. Kim, M. Mikhaylova, F.H. Wang, J. Kehr, B. Bjelke, Y. Zhang, T. Tsakalakos, M. Muhammed, Starch-Coated Superparamagnetic Nanoparticles as MR Contrast Agents, Chem. Mater. 15 (2003) 4343–4351. doi:10.1021/cm031104m.

[38] K. Lagarec, D.G. Rancourt, Recoil - Mössbauer Spectral Analysis Software for Windows, version 1.02, (1998).

[39] L. Vayssières, C. Chanéac, E. Tronc, J.P. Jolivet, Size Tailoring of Magnetite Particles Formed by Aqueous Precipitation: An Example of Thermodynamic Stability of Nanometric Oxide Particles, Journal of Colloid and Interface Science. 205 (1998) 205–212. doi:10.1006/jcis.1998.5614.

[40] D.K. Kim, Y. Zhang, W. Voit, K.V. Rao, M. Muhammed, Synthesis and characterization of surfactant-coated superparamagnetic monodispersed iron oxide nanoparticles, Journal of Magnetism and Magnetic Materials. 225 (2001) 30–36. doi:10.1016/S0304-8853(00)01224-5.

[41] T.J. Daou, G. Pourroy, S. Bégin-Colin, J.M. Grenèche, C. Ulhaq-Bouillet, P. Legaré, P. Bernhardt, C. Leuvrey, G. Rogez, Hydrothermal Synthesis of Monodisperse Magnetite Nanoparticles, Chem. Mater. 18 (2006) 4399–4404. doi:10.1021/cm060805r.

[42] K.W. Andrews, D.J. Dyson, S.R. Keown, Interpretation of Electron Diffraction Patterns, Springer US, 1967.

[43] P. Scherrer, Bestimmung der Größe und der inneren Struktur von Kolloidteilchen mittels Röntgenstrahlen, Nachrichten von der Gesellschaft der Wissenschaften zu Göttingen, Mathematisch-Physikalische Klasse. 1918 (1918) 98–100.

[44] C. Suryanarayana, M.G. Norton, X-Ray Diffraction: A Practical Approach, Springer US, 1998.

[45] D.L.A. de Faria, S. Venâncio Silva, M.T. de Oliveira, Raman microspectroscopy of some iron oxides and oxyhydroxides, J. Raman Spectrosc. 28 (1997) 873–878. doi:10.1002/(SICI)1097-4555(199711)28:11<873::AID-JRS177>3.0.CO;2-B.

[46] O.N. Shebanova, P. Lazor, Raman spectroscopic study of magnetite (FeFe2O4): a new assignment for the vibrational spectrum, Journal of Solid State Chemistry. 174 (2003) 424–430. doi:10.1016/S0022-4596(03)00294-9.

[47] C.S.S.R. Kumar, ed., Raman Spectroscopy for Nanomaterials Characterization, Springer-Verlag, Berlin Heidelberg, 2012.

[48] Y. El Mendili, F. Grasset, N. Randrianantoandro, N. Nerambourg, J.-M. Greneche, J.-F. Bardeau, Improvement of Thermal Stability of Maghemite Nanoparticles Coated with Oleic Acid and Oleylamine Molecules: Investigations under Laser Irradiation, J. Phys. Chem. C. 119 (2015) 10662–10668. doi:10.1021/acs.jpcc.5b00819.

[49] R.E. Vandenberghe, C.A. Barrero, G.M. da Costa, E.V. San, E.D. Grave, Mössbauer characterization of iron oxides and (oxy)hydroxides: the present state of the art, Hyperfine Interactions. 126 (2000) 247–259. doi:10.1023/A:1012603603203.

[50] A. Zegeye, M. Abdelmoula, M. Usman, K. Hanna, C. Ruby, In situ monitoring of lepidocrocite bioreduction and magnetite formation by reflection Mössbauer spectroscopy, American Mineralogist. 96 (2011) 1410–1413. doi:10.2138/am.2011.3794.

[51] J. Fock, M.F. Hansen, C. Frandsen, S. Mørup, On the interpretation of Mössbauer spectra of magnetic nanoparticles, Journal of Magnetism and Magnetic Materials. 445 (2018) 11–21. doi:10.1016/j.jmmm.2017.08.070.

[52] D.G. Rancourt, J.Y. Ping, Voigt-based methods for arbitrary-shape static hyperfine parameter distributions in Mössbauer spectroscopy, Nuclear Instruments and Methods in Physics Research Section B: Beam Interactions with Materials and Atoms. 58 (1991) 85–97. doi:10.1016/0168-583X(91)95681-3.

[53] D.G. Rancourt, Mössbauer spectroscopy in clay science, Hyperfine Interactions. 117 (1998) 3–38. doi:10.1023/A:1012651628508.

[54] L. Néel, Théorie du trainage magnetique des ferromagnetiques en grains fins avec applications aux terres cuites, Ann. Geophys. 5 (1949) 99–136.

[55] C.M. Srivastava, S.N. Shringi, M.V. Babu, Mössbauer study of the low-temperature phase of magnetite, Physica Status Solidi (A). 65 (1981) 731–735. doi:10.1002/pssa.2210650241.

[56] R.S. Hargrove, W. Kündig, Mössbauer measurements of magnetite below the Verwey transition, Solid State Communications. 8 (1970) 303–308. doi:10.1016/0038-1098(70)90455-2.

[57] A.C. Doriguetto, N.G. Fernandes, A.I.C. Persiano, E.N. Filho, J.M. Grenèche, J.D. Fabris, Characterization of a natural magnetite, Phys Chem Minerals. 30 (2003) 249–255. doi:10.1007/s00269-003-0310-x.

[58] S. Mørup, E. Tronc, Superparamagnetic relaxation of weakly interacting particles, Phys. Rev. Lett. 72 (1994) 3278–3281. doi:10.1103/PhysRevLett.72.3278.

[59] F. Bødker, M.F. Hansen, C.B. Koch, K. Lefmann, S. Mørup, Magnetic properties of hematite nanoparticles, Phys. Rev. B. 61 (2000) 6826–6838. doi:10.1103/PhysRevB.61.6826.

[60] J. van Lierop, D.H. Ryan, Mössbauer spectra of single-domain fine particle systems described using a multiple-level relaxation model for superparamagnets, Phys. Rev. B. 63 (2001) 064406. doi:10.1103/PhysRevB.63.064406.

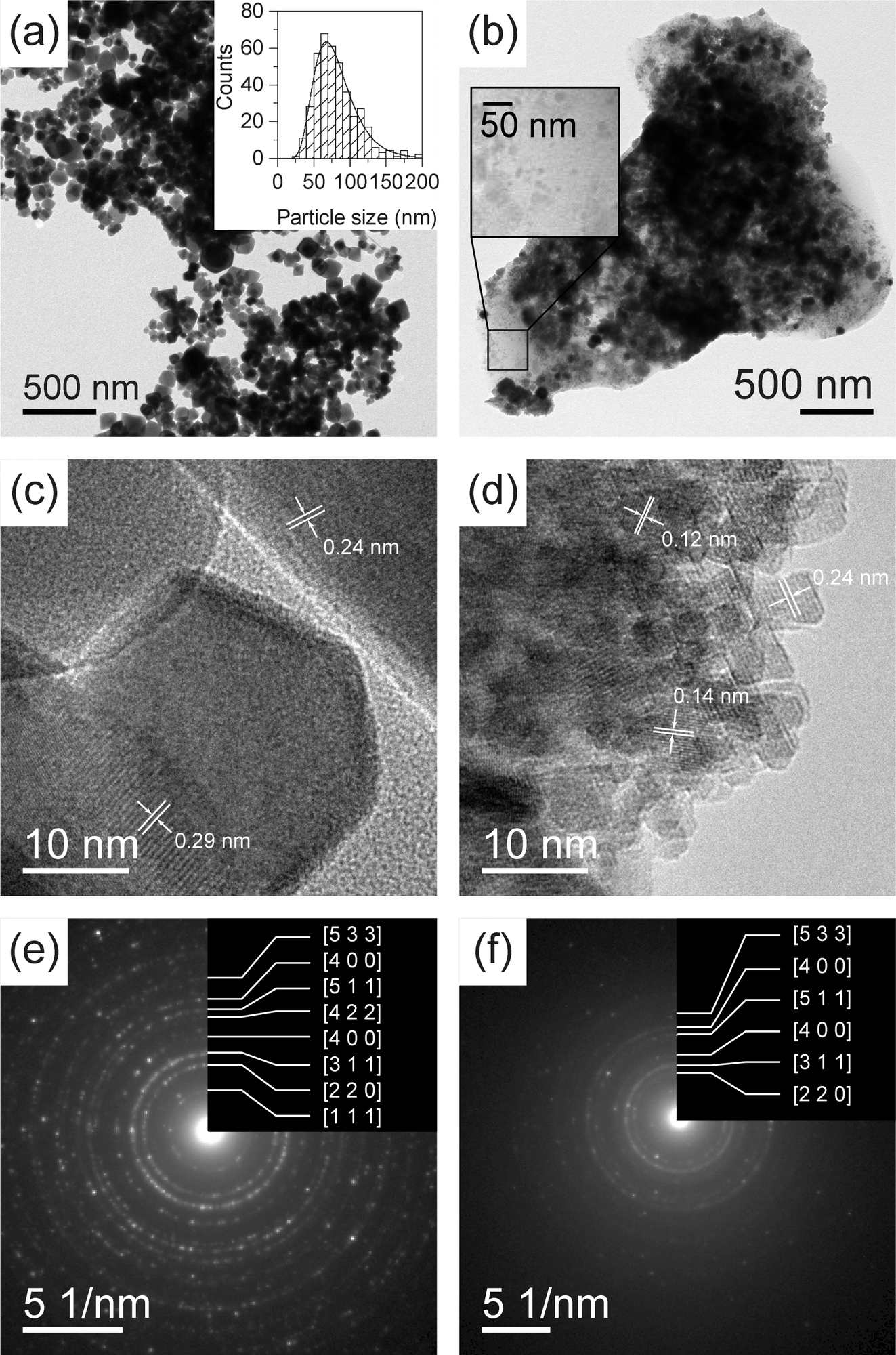
(a)
Counts
80
60
40
20
0
0 50 100 150 200
Particle size (nm)
500 nm
(b)
50 nm
500 nm
(c)
0.24 nm
10 nm
0.29 nm
(d)
0.12 nm
0.24 nm
0.14 nm
10 nm
(e)
[5 3 3]
[4 0 0]
[5 1 1]
[4 2 2]
[4 0 0]
[3 1 1]
[2 2 0]
[1 1 1]
5 1/nm
(f)
[5 3 3]
[4 0 0]
[5 1 1]
[4 0 0]
[3 1 1]
[2 2 0]
5 1/nm

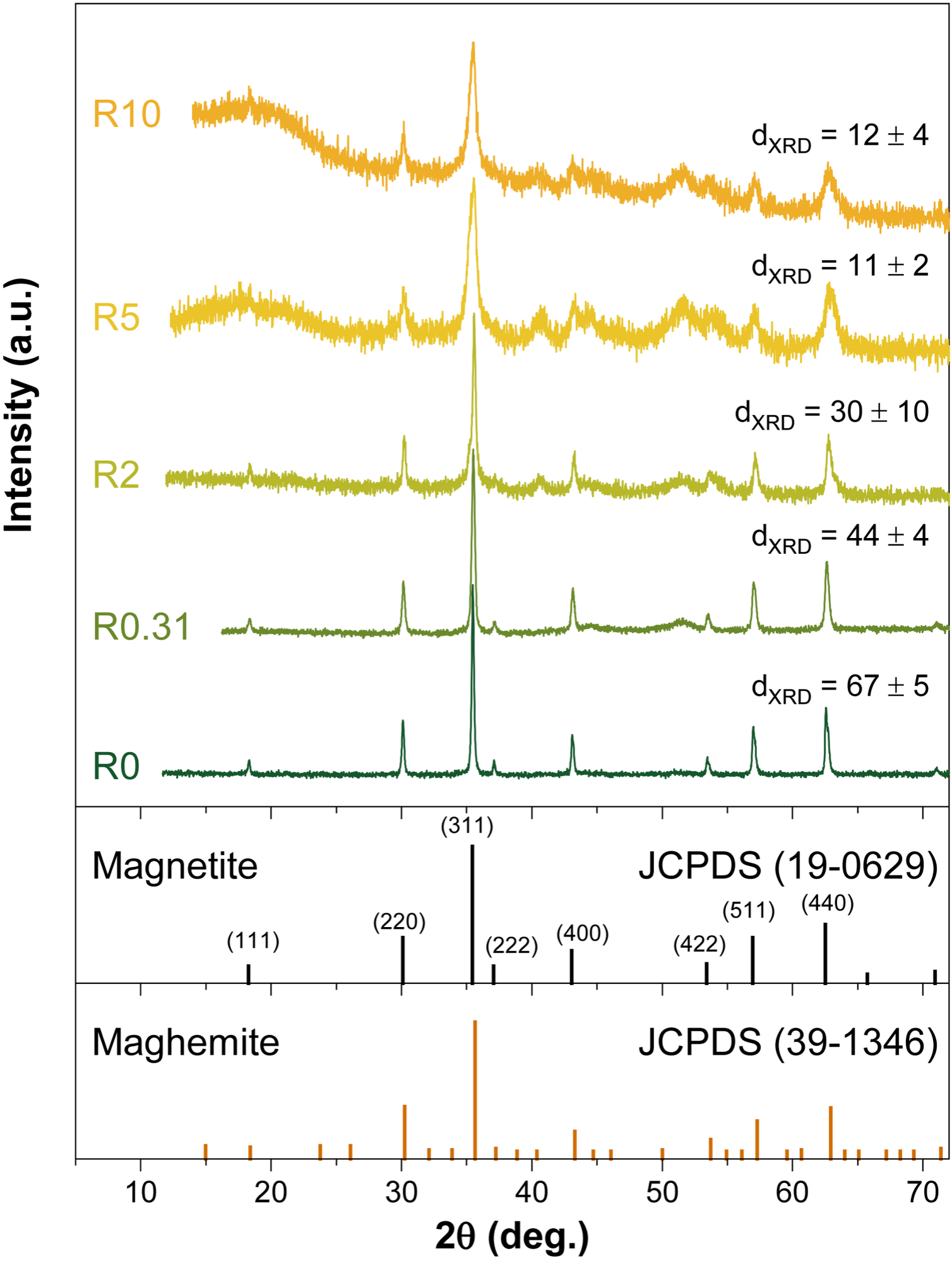
R10
$d_{XRD} = 12 \pm 4$
R5
$d_{XRD} = 11 \pm 2$
R2
$d_{XRD} = 30 \pm 10$
R0.31
$d_{XRD} = 44 \pm 4$
R0
$d_{XRD} = 67 \pm 5$
Intensity (a.u.)
Magnetite
JCPDS (19-0629)
(111)
(220)
(311)
(222)
(400)
(422)
(511)
(440)
Maghemite
JCPDS (39-1346)
10
20
30
40
50
60
70
2θ (deg.)

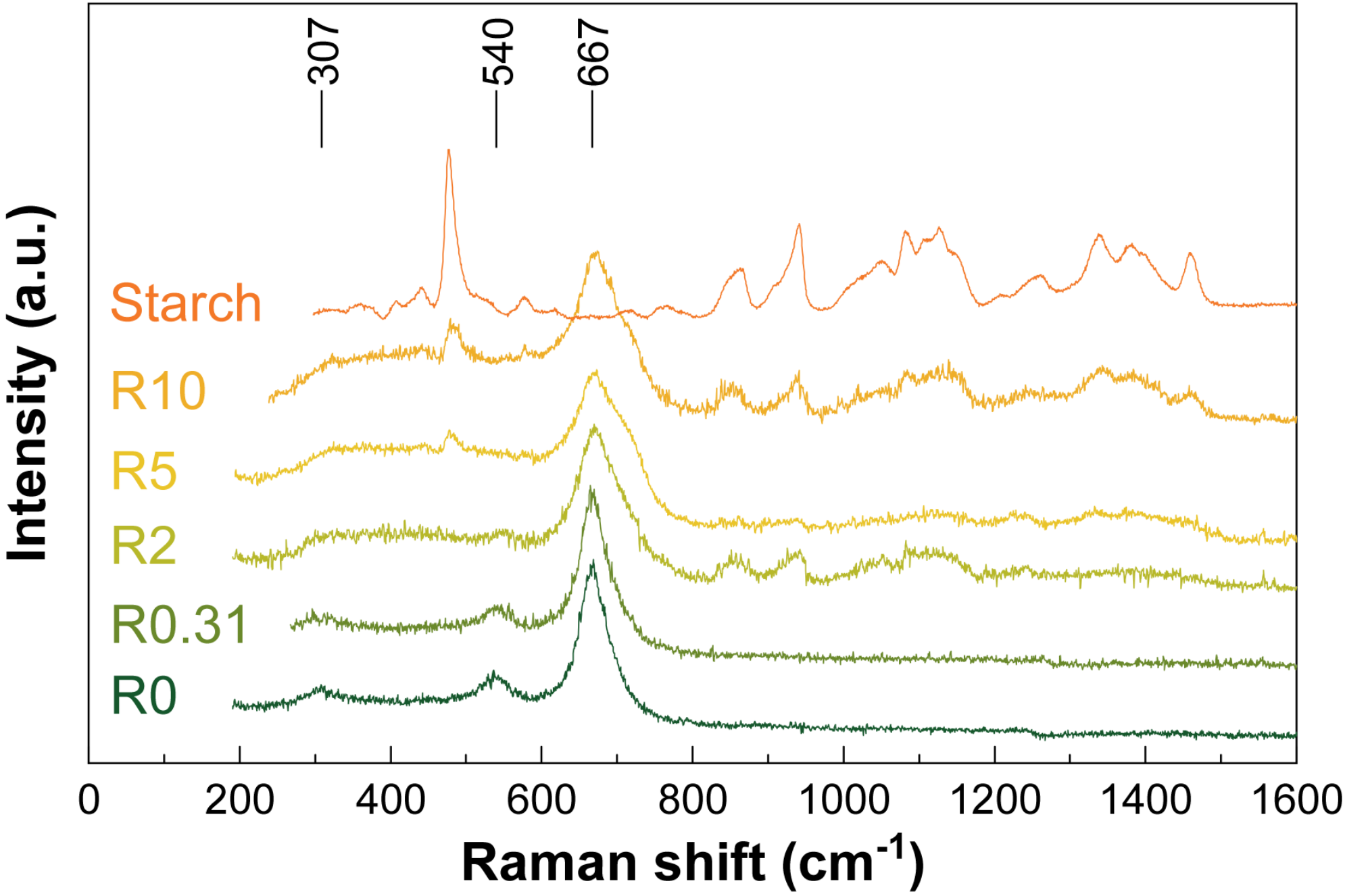
307
540
667
Starch
R10
R5
R2
R0.31
R0
Intensity (a.u.)
0
200
400
600
800
1000
1200
1400
1600
Raman shift (cm-1)

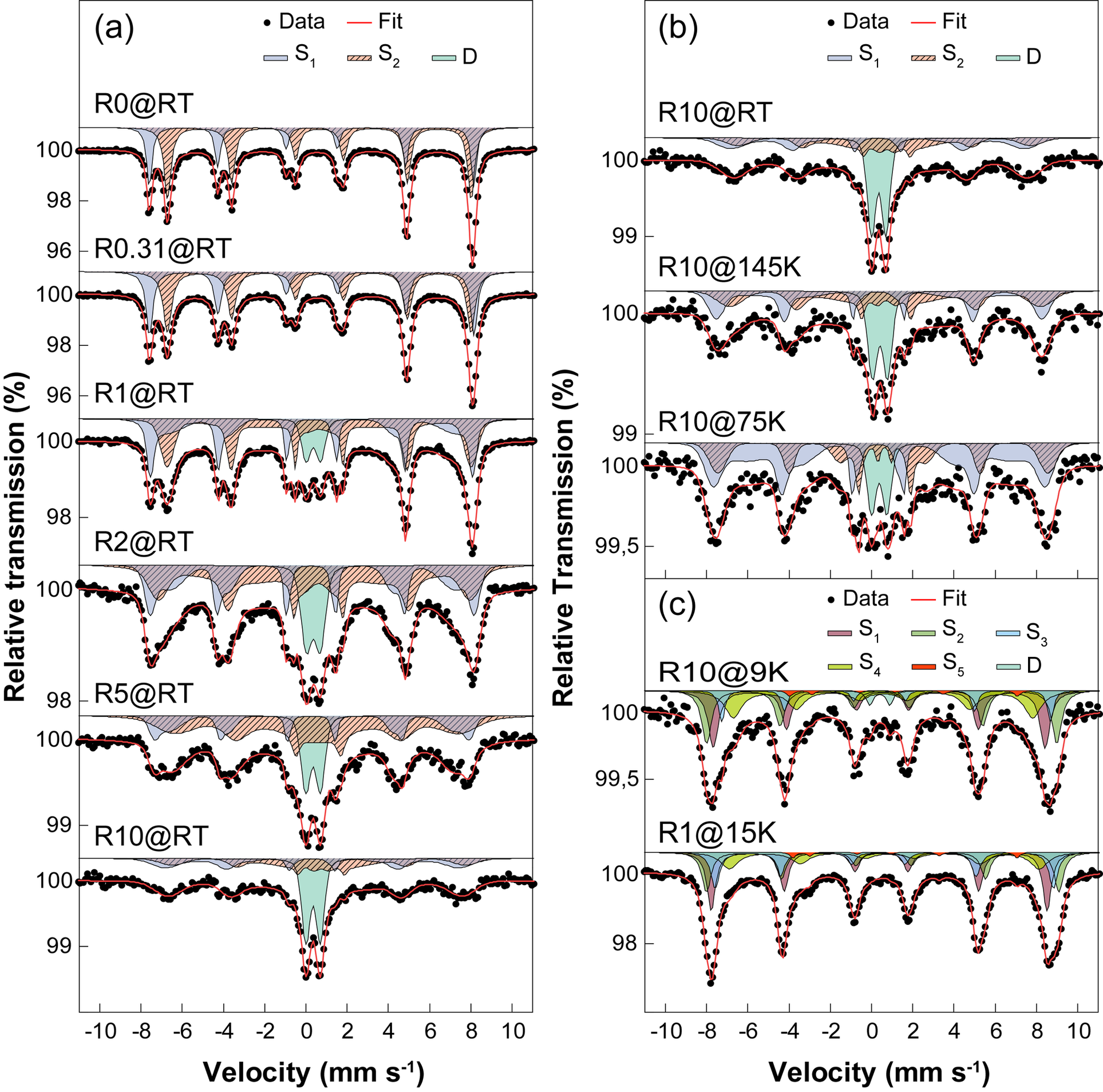
(a)
Data
Fit
S1
S2
D
R0@RT
R0.31@RT
R1@RT
R2@RT
R5@RT
R10@RT
Relative transmission (%)
Velocity (mm s-1)
(b)
R10@RT
R10@145K
R10@75K
Relative Transmission (%)
(c)
S3
S4
S5
R10@9K
R1@15K

Evolution of magnetite crystallite size with the starch to iron mass ratio R (left) and room temperature Mössbauer spectra of the as-synthetized products showing the gradual increase of the superparamagnetic doublet with R (right)

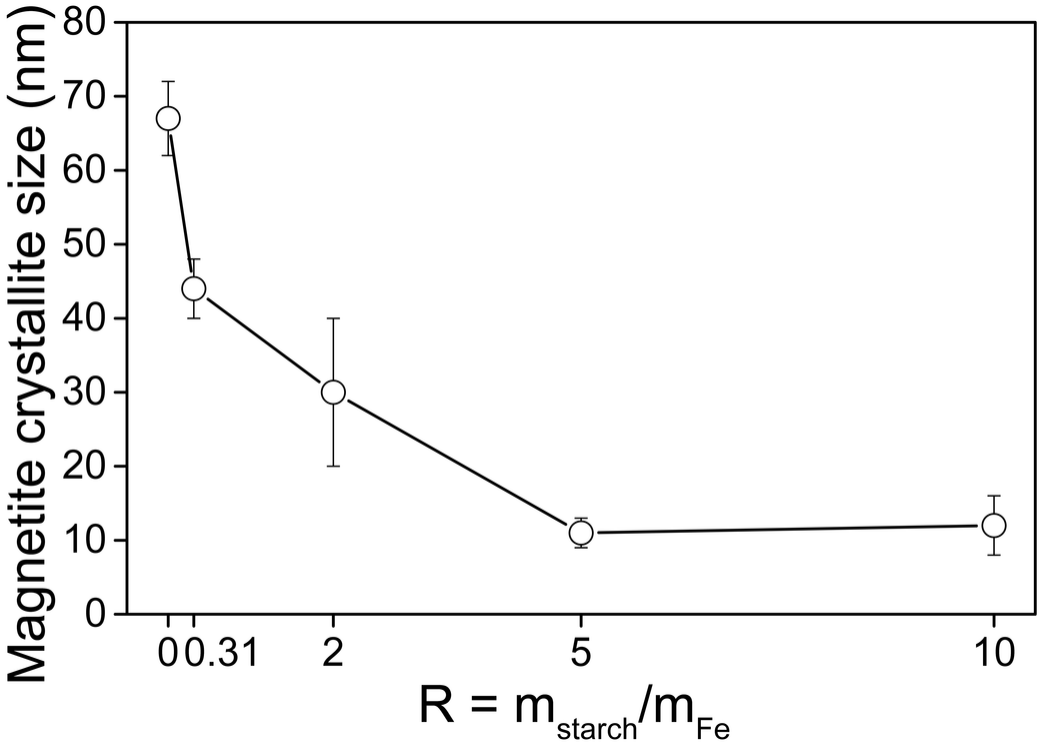
Magnetite crystallite size (nm)
0
10
20
30
40
50
60
70
80
0
0.31
2
5
10
R = m_starch/m_Fe

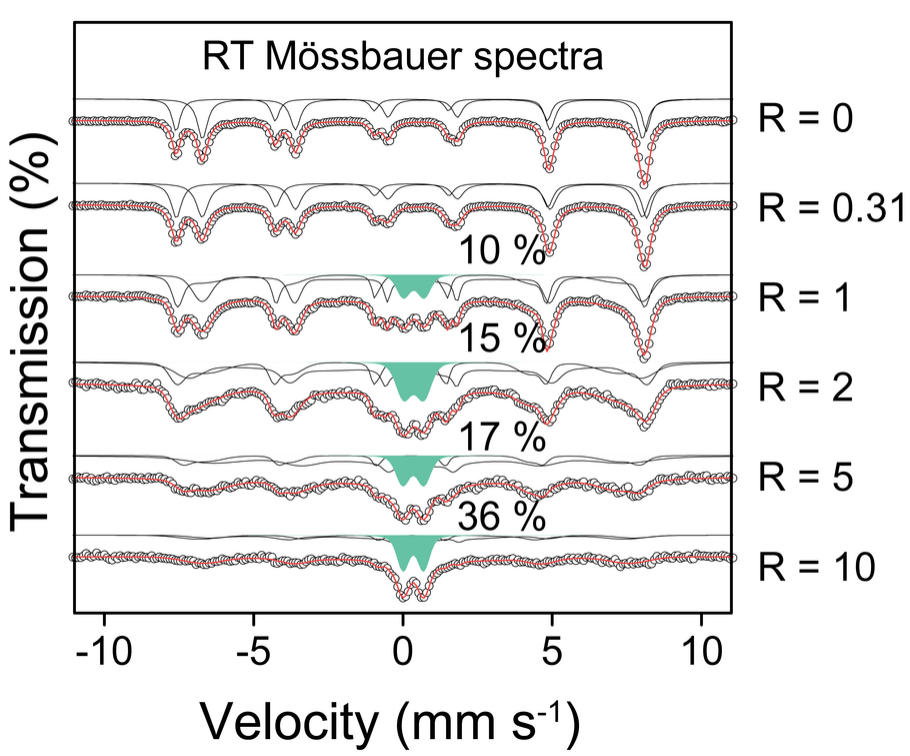
RT Mössbauer spectra
Transmission (%)
R = 0
R = 0.31
10 %
R = 1
15 %
R = 2
17 %
R = 5
36 %
R = 10
-10
-5
0
5
10
Velocity (mm s-1)